The Monopole-Source Solution for Estimating Tissue Temperature Increases for Focused Ultrasound Fields

D. Scott Ellis and William D. O'Brien, Jr., *Fellow, IEEE*

***Abstract*—The monopole-source solution to the problem of estimating tissue temperature rise generated by a focused ultrasound beam is presented. The acoustic pressure field generated by a focused, continuous-wave ultrasound source using the acoustic monopole-source method is developed. The point-source solution to the linear bio-heat transfer equation is used to calculate the axial, steady-state temperature increase for both circular and rectangular apertures. The results of the circular aperture are compared with the temperature increase calculated using the heated-disc method and are shown to be in substantial agreement. Finally, the temperature increase generated by the circular aperture is compared to that of the rectangular aperture for the same source power, aperture surface area, operating frequency, and medium properties, and it is shown that the rectangular source generates temperature increases less than those of the circular source under these conditions.**

I. Introduction

THE determination of tissue heating from exposure to ultrasound under diagnostic exposure conditions is of great importance for assessing risk. It is well known that biological effects occur due to temperature increases and that thermally produced bioeffects are both temperature and time dependent [1].

While it must be stressed that there has never been a confirmed biological effect report in humans due to diagnostic ultrasound over the last four decades, the ability to estimate quantitatively the temperature elevation in tissue is far from complete. With a more accurate means to estimate temperature elevation, it may be possible to operate diagnostic ultrasound equipment at even output levels higher than presently allowed by the FDA [2], [3] and still not increase patient risk. Substantial efforts have been made to develop simple mathematical models of ultrasound beams and the resulting temperature elevation in tissue [4]–[13]. Several committee reports have been published in recent years addressing ultrasonic tissue heating, as well as the mathematical models available to determine quantitatively what is believed to be "worst-case" levels of tissue heating [14]–[16]. In addition, the Output Display Standard [17] has introduced methodology by which manufacturers provide various "Thermal Indices" to the operator of diagnostic ultrasound equipment in order to provide information related to potential temperature increases attainable under the specific operating conditions of the ultrasonic imaging system.

This paper presents a general method which does not restrict itself to a specific beam geometry, and thus has applicability to any arbitrarily shaped source aperture. In addition, the monopole-source solution method is not restricted to calculating the temperature increase only at points on the beam axis but is applicable for locations anywhere in the field.

Manuscript received February 21, 1994; revised August 1, 1995. This work was supported in part by the National Center for Supercomputing Applications and NIH Grants CA09067 and HD21687.

The authors are with the Bioacoustics Research Laboratory, Department of Electrical and Computer Engineering, University of Illinois at Urbana-Champaign, Urbana, IL 61801 USA.

Publisher Item Identifier S 0885-3010(96)00363-2.

II. Theory

The monopole-source solution, which consists of two independent steps, has been developed to determine tissue heating. The first step determines the 3-D acoustic pressure field generated by an ultrasonic source. The second step uses the 3-D acoustic pressure field to determine the temperature increase at any point in the medium. Both of these steps will be presented.

A. Acoustic Monopole

The monopole-source solution is used to evaluate the spatial distribution of the complex acoustic pressure, $\mathbf{p}$, from an aperture of arbitrary geometry, where $\mathbf{p}$ is determined from the lossy Helmholtz equation given by

$$\nabla^2\mathbf{p} + \mathbf{k}^2\mathbf{p} = 0 \tag{1}$$

where $\mathbf{k}$ is the complex wave number ($\mathbf{k} = k_0 - j\alpha$), and where k_0 and α are the wave number (ω/c) and amplitude absorption coefficient, respectively. If the acoustic source is very small and spherically symmetric (a monopole source) with angular frequency ω in an unbounded fluid, the monopole-source solution to the Helmholtz equation gives rise to an outgoing spherically symmetric wave where

$$\mathbf{p} = G\frac{\exp(-j\mathbf{k}r)}{r} = G\frac{\exp(-\alpha r)\exp(-jk_0 r)}{r} \tag{2}$$

where the constant G is called the monopole-pressure amplitude and the outgoing radial distance r is given by

$$r = \sqrt{(x_1 - x_0)^2 + (y_1 - y_0)^2 + (z_1 - z_0)^2}. \tag{3}$$

In Cartesian coordinates, (x_0, y_0, z_0) is the location in space of the monopole source and (x_1, y_1, z_1) is the observation location.

The spatial distribution of acoustic pressure from a source aperture of arbitrary geometry with N acoustic monopoles is determined by applying the superposition principle. Thus, the

complex pressure $\mathbf{p}$ at field location (x_1, y_1, z_1) is determined as

$$\begin{aligned}\mathbf{p}(x_1, y_1, z_1) &= G\sum \frac{\exp(-Ar)\exp(-jkr)}{r} \\ &= G\mathbf{p}_{\rm rel}(x_1, y_1, z_1)\end{aligned} \tag{4}$$

where the absorption coefficient α has been replaced by the attenuation coefficient A to account for the fact that the loss of amplitude as the wave propagates is quantified by the attenuation coefficient, whereas the absorption coefficient is a quantitative representation of the propagated loss of energy into heat.

The square of the acoustic pressure amplitude at field location (x_1, y_1, z_1) is calculated from

$$\begin{aligned}p_0^2 &= \mathbf{p}(x_1, y_1, z_1)\mathbf{p}^*(x_1, y_1, z_1) \\ &= G^2\mathbf{p}_{\rm rel}(x_1, y_1, z_1)\mathbf{p}^*_{\rm rel}(x_1, y_1, z_1)\end{aligned} \tag{5}$$

where $\mathbf{p}^*$ denotes the complex conjugate of $\mathbf{p}$. The value of $G^2(z)$ is determined at the axial distance z from a known temporal-average source power $W_{\rm SOURCE}$ (at $z = 0$)

$$G = \frac{W_{\rm SOURCE}\exp(-2Az)}{\sum_{xy}\frac{\langle \mathbf{p}_{\rm rel}\mathbf{p}^*_{\rm rel}\rangle}{\rho c}\Delta x\Delta y} \tag{6a}$$

where $\langle \mathbf{p}_{\rm rel}\mathbf{p}^*_{\rm rel}\rangle$ values are summed over an x–y plane perpendicular to the z-axis (the beam axis) at range z. The numerator of (6a) is the derated power at distance z from the source and the denominator is the relative power in that plane from the computed pressure field. For sinusoidal waves only, the denominator can be replaced with

$$\sum_{xy}\frac{\mathbf{p}_{\rm rel}\mathbf{p}^*_{\rm rel}}{2\rho c}\Delta x\Delta y. \tag{6b}$$

B. Bio-Heat Transfer Equation

In the mathematical modeling of the temperature increase generated by ultrasound, the bio-heat transfer equation is used to combine the processes of ultrasonic absorption, tissue perfusion, and heat conduction [18], [19], that is,

$$\frac{\partial T}{\partial t} = \kappa\nabla^2 T - \frac{\Delta T}{\tau} + \frac{q_v}{\rho c_p} \tag{7}$$

where T is the ambient temperature level, κ is the thermal diffusivity, ΔT is the temperature elevation, τ is the perfusion time constant, and c_p is the heat capacity per unit mass of the medium. For continuous-wave (cw) ultrasound propagated in an absorbing medium, heat is generated locally at a temporal-average rate per unit volume by the expression [6], [13]

$$q_v = \frac{\alpha p_0^2}{\rho c} \tag{8}$$

where ρc is the medium's characteristic acoustic impedance (product of density, ρ, and propagation speed, c).

A solution to (7) is used as the basis for the monopole-source solution to yield the temperature increase as a function of time, t, at a distance r from an infinitesimal heat source of volume dv which is generating heat at a rate $q_v dv$ [18], that is,

$$\Delta T(t, r) = \frac{C}{r}\{E[2 - \operatorname{erfc}(t^* - R)] + E^{-1}\operatorname{erfc}(t^* + R)\} \tag{9}$$

where

$$C = \frac{q_v dv}{8\pi K} = \frac{\alpha p_0^2 dv}{8\pi\rho c K} \tag{9a}$$

$$K = \rho c_p \kappa \tag{9b}$$

$$E = \exp(-r/L) \tag{9c}$$

$$L = \sqrt{\kappa\tau} \tag{9d}$$

$$t^* = \sqrt{t/\tau} \tag{9e}$$

$$R = r/\sqrt{4\kappa\tau} \tag{9f}$$

and where K is the thermal conductivity coefficient, L is the perfusion length, and erfc is the compliment of the error function. The steady-state solution for (9) is

$$\Delta T(r) = \frac{2C}{r}\exp\Big(-\frac{r}{L}\Big) \tag{10}$$

and this point-source solution to the bio-heat transfer equation is used as the basis for determining the steady-state temperature increase in tissue exposed to ultrasound reported herein.

C. Axial Temperature Increase: Heated Point-Source Method

From the p_0^2 field distribution (5), the axial temperature increase along the z-axis can be calculated. Using the point-source solution (10) to the bio-heat transfer equation, the steady-state temperature increase at an observation point $P_{\rm obs}(x_{\rm obs}, y_{\rm obs}, z_{\rm obs})$ due to a heated point-source located at $P_{\rm hs}(x_{\rm hs}, y_{\rm hs}, z_{\rm hs})$ is given by [18]

$$\Delta T(P_{\rm obs}, P_{\rm hs}) = \frac{2C}{s}\exp\Big(-\frac{s}{L}\Big) \tag{11}$$

where s is the distance between $P_{\rm obs}(x_{\rm obs}, y_{\rm obs}, z_{\rm obs})$ and $P_{\rm hs}(x_{\rm hs}, y_{\rm hs}, z_{\rm hs})$. The steady-state temperature increase along the z-axis ($z_{\rm obs}$ locations) is calculated, using the superposition principle, by summing the incremental temperature increases, $\Delta T(P_{\rm obs}, P_{\rm hs})$, from every heated point-source location $(P_{\rm hs})$ in the medium to the observation locations $(P_{\rm obs})$, that is,

$$\Delta T_{\rm AXIAL}(z_{\rm obs}) = \sum_{xyz}\Delta T(P_{\rm hs}(x, y, z), P_{\rm obs}(0, 0, z_{\rm obs})). \tag{12}$$

D. Axial Temperature Increase: Heated-Disc Method

Another method used to determine the temperature increase along the beam axis is the heated-disc method [15], [16]. In this method, the ultrasound beam is modeled as a series of discs, each centered on the beam axis, whose diameter is equal to the beam width at each axial distance and whose intensity is uniform over the disc and zero elsewhere. In addition, q_v is uniform over the disc surface because the intensity distribution is uniform over the disc surface.

The beam width used in the heated-disc approach is mathematically given by Kossoff [20] and modified [15] to correspond to the 6-dB beam width. The beam width is defined as the distance, off-axis, between the points with magnitude 6 dB below the maximum intensity in that plane [15]. A dimensionless quantity Ψ is used to define the beam width,

$w(z)$, where

$$\Psi = \frac{\pi D^2 |\mathrm{ROC} - z|}{8\lambda \mathrm{ROC} z} \tag{13}$$

$$w(z) = D\left[1 - \frac{z}{\mathrm{ROC}}\right] \qquad \text{for } \Psi > 2.56 \tag{14a}$$

$$w(z) = \frac{0.55 D |\mathrm{ROC} - z|}{\mathrm{ROC} \sin \Psi} \qquad \text{for } \Psi < 2.56 \tag{14b}$$

where ROC is the radius of curvature, D is the diameter, and λ is the acoustic wavelength.

The intensity at each point on the disc is given as the power contained in the cross section, W_{CS}, divided by the cross-sectional area, A_{CS}, of the beam. In the heated-disc method, all of the power is defined to exist within the given beam width and is equal to the derated power at the axial distance, z, from the transducer. The cross section is a disc with diameter equal to the beam width, $w(z)$, that is,

$$I_{\mathrm{SATA}}(z) = \frac{W_{\mathrm{CS}}(z)}{A_{\mathrm{CS}}} = \frac{W_0 \exp(-2Az)}{\pi w^2(z)/4} \tag{15}$$

where $I_{\mathrm{SATA}}(z)$ is the spatial-average temporal-average intensity at the axial distance z.

The steady-state temperature increase generated on the disc axis a distance ζ from the disc is given by (see [15, App. B] for derivation),

$$\Delta T_{\mathrm{DISC}}(\zeta) = \frac{2\alpha I_{\mathrm{SATA}} \varepsilon L}{2K} [\exp(-\zeta/L) - \exp(-r'/L')] \tag{16}$$

where ε is the disc thickness and r' is $\sqrt{(w/2)^2 + \zeta^2}$. This equation was obtained by integrating (11) over the surface area of the heated disc [15].

The temperature increase at an individual point on the beam axis is determined by superimposing the temperature increases due to each disc on the beam axis. Thus, the axial steady-state temperature increase is given as

$$\Delta T_{\mathrm{AXIAL}}(z_{\mathrm{obs}}) = \sum_z \Delta T_{\mathrm{DISC}}(z - z_{\mathrm{obs}}). \tag{17}$$

III. Methods

A. Heated-Disc

The heated-disc method requires the evaluation of (13) and (14) to determine the beam width for the specific case of a circular aperture (Fig. 1). Using the beam width, the spatial-average temporal-average intensity is then computed using (15). Finally, the axial temperature increase is calculated using (17). The only computational simulation parameter required is ε. For this paper, the specific tissue and ultrasound source properties studied for the heated-disc method are given in Table I. The simulation parameter ε is 0.01 cm. The summation in (17) is evaluated for $|z - z_{\mathrm{obs}}| \leq 3L$ [18].

B. Monopole-Source

The monopole-source method requires that the 3-D complex pressure field, $\mathbf{p}$, be determined at every point in the medium [see (4)]. In modeling the acoustic monopole sources, the area of each monopole source is $(\lambda/4)^2$ and the monopole-source amplitude is the same for all monopole sources. The field spacing for the points in the medium is 0.01 cm and, hence, the volume of a field voxel is (0.01 cm)^3 (see Sections IV and V). Once the relative complex pressure field has been determined, the monopole-source amplitude is determined [see (6)], where the summation is over the x–y plane perpendicular to the beam axis, at a range z. Finally, (12) is used to determine the temperature increase at a point on the beam axis. This summation includes all points within three perfusion lengths of each heated point-source [18].

For the circular source aperture, the source power, aperture surface area (see Fig. 1), operating frequency, and medium properties were the same as for the heated-disc case (see Table I). The beam width, $w(z)$, was defined for each distance z, as the lateral distance between the farthest points off-axis that were greater than or equal to 10 dB below the maximum intensity value in that plane. The spatial-average temporal-average intensity (I_{SATA}) was calculated using (15) with A_{CS} defined as a disc with radius equal to $w(z)/2$.

The aperture parameters for the three rectangular cases (see Fig. 2) studied are listed in Table II. The aspect ratio (AR) is defined as the ratio of x_{width} to y_{width}. The same frequency and medium characteristics as those listed in Table I were

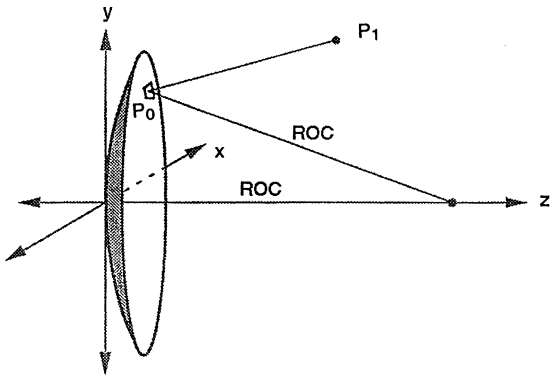

Fig. 1. Geometrical model of a focused circular aperture. The coordinates on the surface of the source, P_0, are (x_0, y_0, z_0) and the coordinates in the medium, P_1, are (x_1, y_1, z_1). ROC denotes the radius of curvature and the beam axis is the z-axis.

TABLE I
Parameters for Heated-Disc and Monopole-Source Simulations

Symbol	Quantity	Value
f	frequency	3 MHz
W_{SOURCE}	source power	100 mW
D	source diameter	2 cm
ROC	radius of curvature	10 cm
c	propagation speed	1540 m/s
A,α	attenuation=absorption	0.15 Np/cm (1.30 dB/cm)
ρ	tissue density	1000 kg/m^3
L	perfusion length	1.18 cm
K	thermal conductivity	0.006 W/cm^2

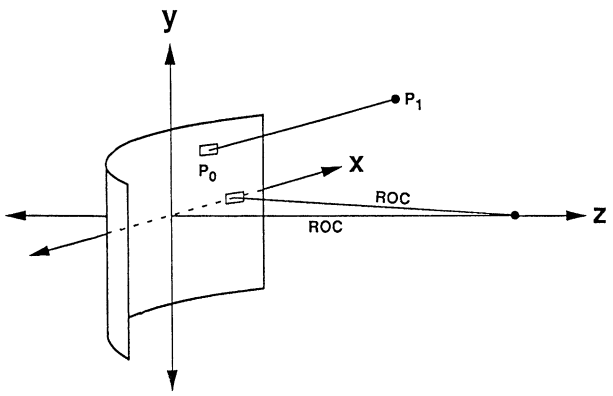

Fig. 2. Geometrical model of a focused rectangular aperture. The coordinates on the surface of the source, P_0, are (x_0, y_0, z_0), and the coordinates in the medium, P_1, are (x_1, y_1, z_1). ROC denotes the radius of curvature and the beam axis is the z-axis.

TABLE II
ASPECT RATIO AND TEMPERATURE PROFILE DATA FOR THE RECTANGULAR APERTURE CASES

Aspect Ratio	x_{width} (cm)	y_{width} (cm)	ΔT_{max}(°C)	ΔT_{max} range (cm)
1	1.7725	1.7725	0.447	1.02
π	3.14	1.00	0.394	1.06
2π	4.44	0.707	0.321	1.04

used. Also, for all three rectangular aperture cases, the surface area of the aperture was held constant to a value of π cm^2, the same surface area used for the circular aperture. In addition, the same radius of curvature (ROC) of 10 cm in the imaging plane was used for each of the rectangular aperture cases. Thus, the f numbers $(=\mathrm{ROC}/D)$ in the imaging plane for these three cases were 6.64, 3.18, and 2.27 for the aspect ratios of 1, π, and 2π, respectively. For the rectangular aperture, two orthogonal beam widths were defined, $w_x(z)$ in the imaging plane (x–z plane) and $w_y(z)$ in the elevational plane (y–z plane). The cross-sectional area was defined as a rectangle with dimensions equal to the 10-dB beam width in the x–z and y–z planes $(A_{\mathrm{CS}} = w_x(z)w_y(z))$. Thus, the spatial-average temporal-average intensity for the rectangular aperture was defined by (15).

IV. RESULTS

A. Monopole-Source Solution: Simulation Parameters

The effect of the size of the monopole source on the resulting axial temperature increase was studied by varying the area of the monopole source for the same transducer and medium characteristics (see Table I) with the exception that $L = 1.0$ cm and $A = \alpha = 0.9$ dB/cm. Fig. 3(a) shows the axial temperature increase for three spacings of the monopole sources, λ/2, λ/4, and λ/6. Fig. 3(b) and (c) shows the axial temperature increase difference relative to the λ/4 monopole-source spacing temperature increase.

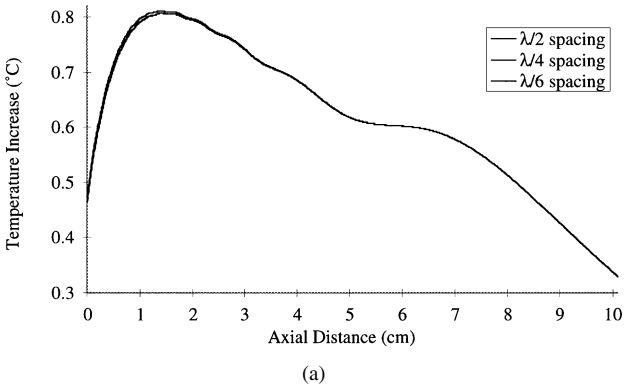

(a)

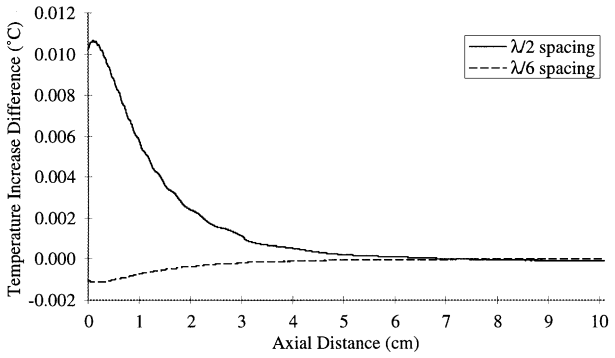

(b)

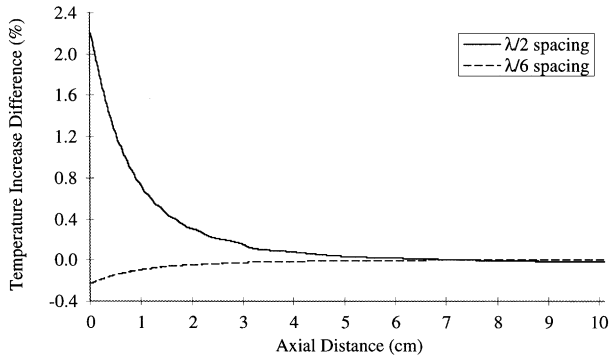

(c)

Fig. 3. (a) Axial temperature increase for a 3-MHz focused circular aperture with diameter of 2 cm, ROC of 10 cm, and source power of 100 mW for three different monopole-source spacings of λ/2, λ/4, and λ/6, that is, monopole-source areas of $(\lambda/2)^2$, $(\lambda/4)^2$, and $(\lambda/6)^2$. The medium is modeled as listed in Table I with the exception that $L = 1.0$ cm and $A = \alpha = 0.9$ dB/cm; the field spacing is 0.01 cm. (b) and (c) Axial temperature increase difference relative to the λ/4 monopole-source spacing temperature increase. The maximum difference between λ/2 and λ/4 is 2.2%, and between λ/6 and λ/4 is -0.22%.

A second modeling issue is that of the sampling size of the medium. Fig. 4(a) shows the axial temperature increase for the same transducer and medium characteristics (see Table I) with the exception that $L = 1.0$ cm and $A = \alpha = 0.9$ dB/cm using a monopole-source spacing of λ/4 and two different field spacings: 0.005 and 0.10 cm. Fig. 4(b) and (c) shows the difference in the axial temperature increase profiles generated when comparing a field spacing of 0.01 cm to that of four different field spacings: 0.005, 0.02, 0.05, and 0.10 cm. In

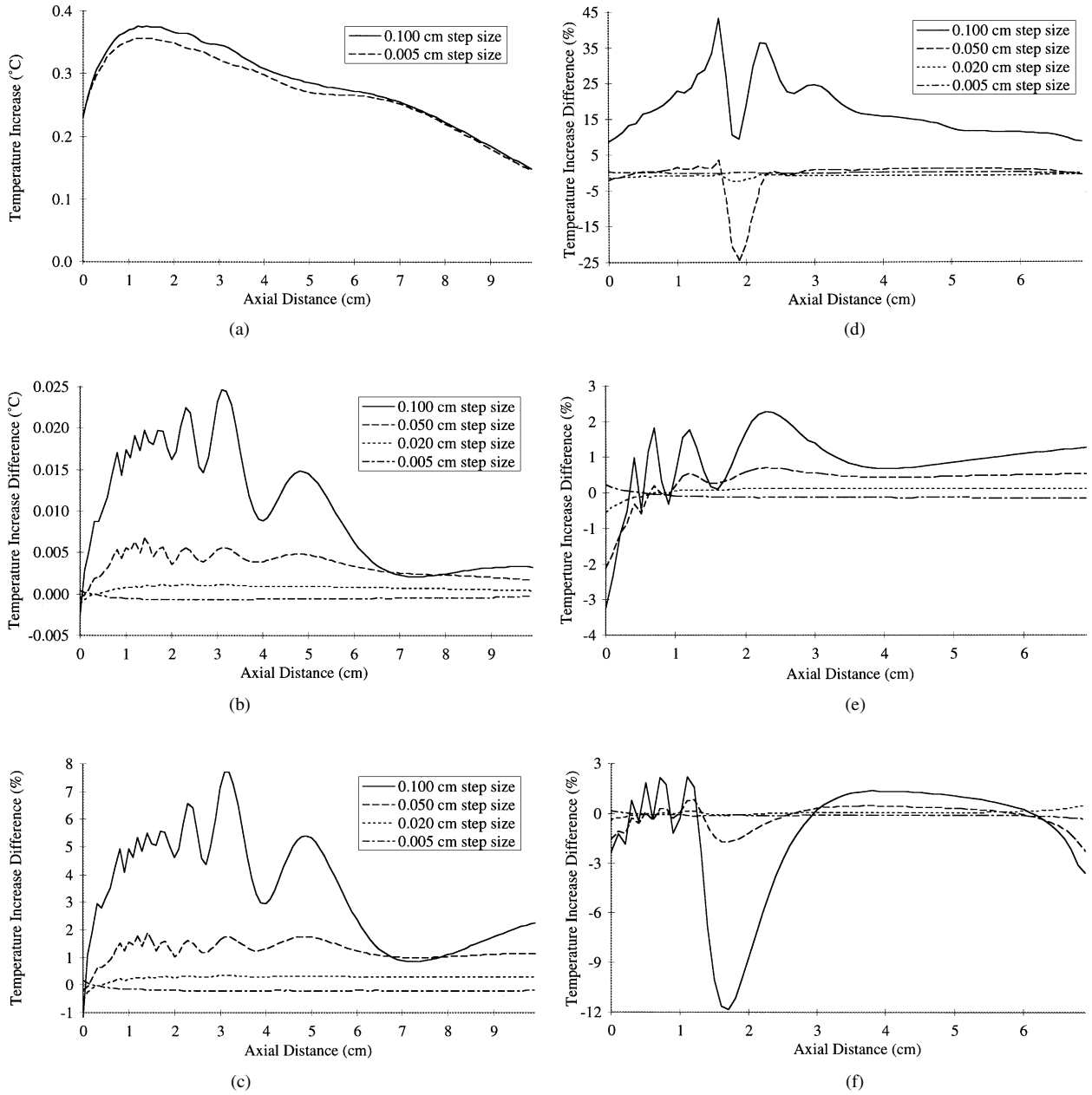

Fig. 4. (a) The axial temperature increase for a 3-MHz focused circular aperture with diameter of 2 cm, ROC of 10 cm, and source power of 100 mW for two different field spacings is 0.100 and 0.005 cm, that is, field voxel volumes of $(0.100\text{ cm})^3$ and $(0.005\text{ cm})^3$. The axial temperature increase profiles for field spacings of 0.050, 0.020, and 0.010 cm fell between those of 0.100 and 0.005 cm. The medium is modeled as listed in Table I with the exception that $L = 1.0$ cm and $A = \alpha = 0.9$ dB/cm (0.3 dB/cm-MHz). The monopole-source spacing is $\lambda/4$. (b) and (c) The axial temperature increase difference relative to the 0.010-cm field spacing temperature increase. Maximum difference between 0.100 and 0.010 cm is 7.7%, between 0.050 and 0.010 cm is 1.9%, between 0.020 and 0.010 cm is 0.35%, and between 0.005 and 0.010 cm is -0.22%. Axial temperature increase difference relative to the 0.010-cm field spacing temperature increase (d) for a 3-MHz focused circular aperture and ROC of 2 cm $(f/1)$ for which the maximum difference between 0.100 and 0.010 cm is 43%, between 0.050 and 0.010 cm is -24%, between 0.020 and 0.010 cm is -2.5%, and between 0.005 and 0.010 cm is -0.25%; (e) for a 1-MHz focused circular aperture and ROC of 10 cm $(f/5)$ for which the maximum difference between 0.100 and 0.010 cm is -3.2%, between 0.050 and 0.010 cm is -2.1%, between 0.020 and 0.010 cm is -0.54%, and between 0.005 and 0.010 cm is 0.21%; (f) for a 1-MHz focused circular aperture and ROC of 2 cm $(f/1)$ for which the maximum difference between 0.100 and 0.010 cm is -12%, between 0.050 and 0.010 cm is -2.2%, between 0.020 and 0.010 cm is 0.60%, and between 0.005 and 0.010 cm is -0.30%. For (d), (e), and (f), the monopole-source spacing is $\lambda/4$, the source diameter is 2 cm, the source power is 100 mW, and the medium is modeled as listed in Table I with the exception that $L = 1.0$ cm and $A = \alpha = 0.3$ dB/cm-MHz.

addition to the specific transducer under study, the effect of the field spacing for three other transducers was evaluated. Fig. 4(d)–(f) shows the axial temperature increase differences for the above-specified field spacings for [Fig. 4(d)] $f = 3$ MHz, $\mathrm{ROC} = 2$ cm, [Fig. 4(e)] $f = 1$ MHz, $\mathrm{ROC} = 10$ cm, and [Fig. 4(f)] $f = 1$ MHz, $\mathrm{ROC} = 2$ cm. For these cases, $A = \alpha = 0.3$ dB/cm-MHz.

B. Heated-Disc Solution: Circular Source Aperture

The heated-disc method was used to compute the axial temperature increase for a circular aperture with a homogeneous tissue model (see Table I). Fig. 5 (dashed lines) shows the 10-dB beam width as a function of axial distance (15), the axial spatial-average temporal-average intensity (16), and the axial temperature increase (17) for the heated-disc model.

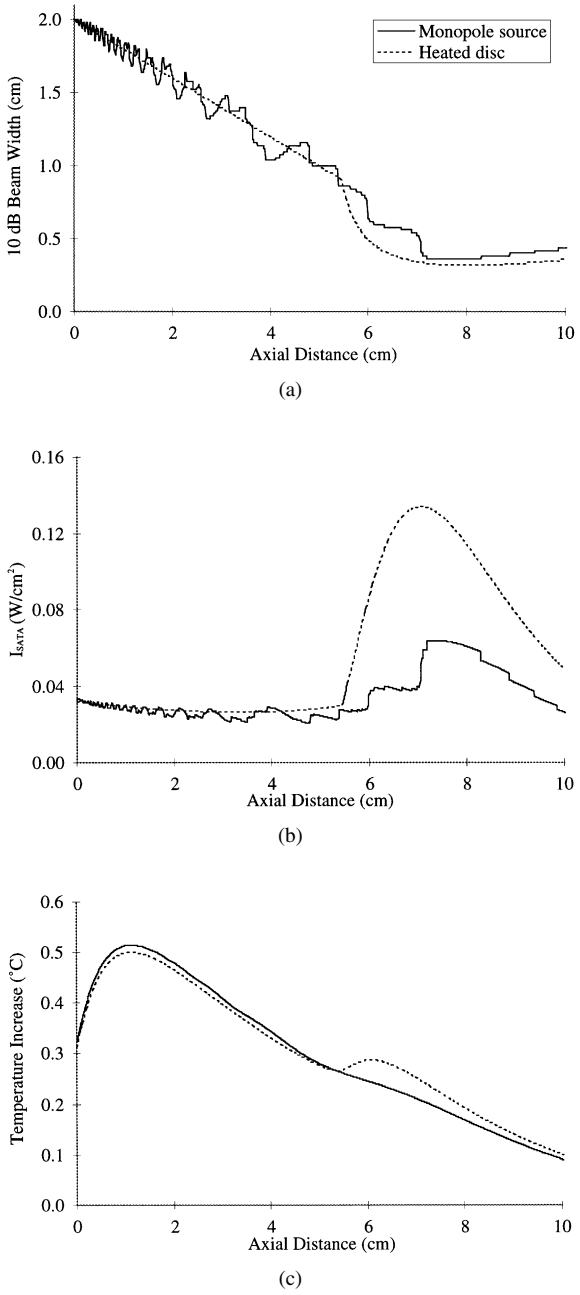

Fig. 5. The (a) 10-dB beam width as a function of axial distance, (b) axial spatial-average temporal-average intensity, and (c) axial temperature increase calculated from the monopole-source and the heated-disc solutions. The source and homogeneous tissue medium quantities are listed in Table I.

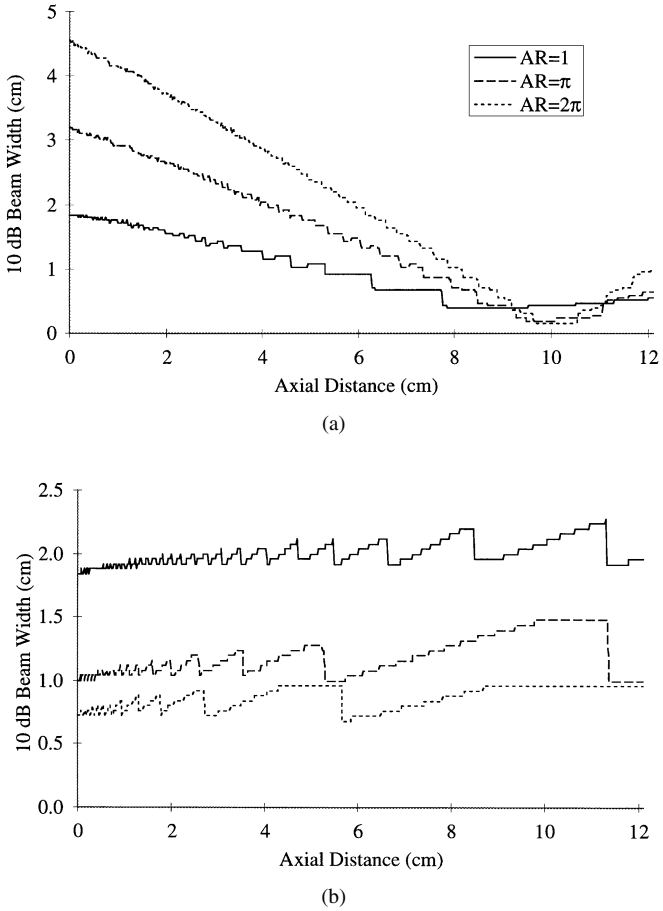

Fig. 6. The 10-dB beam width as a function of axial distance in the (a) imaging plane (x–z plane) and (b) elevational plane (y–z plane) calculated from the monopole-source solution for the three aspect ratio (AR) rectangular aperture cases. The source and homogeneous tissue medium quantities are listed in Table I save for the source diameter. The rectangular source aperture dimensions are listed in Table II.

C. Monopole-Source Solution: Circular Source Aperture

Fig. 5 (solid lines) shows the 10-dB beam width as a function of axial distance, axial spatial-average temporal-average intensity, and axial temperature increase. The source and homogeneous tissue medium quantities are listed in Table I.

D. Monopole-Source Solution: Rectangular Source Aperture

Fig. 6(a) and (b) shows the computed 10-dB beam width as a function of axial distance in the imaging plane, $w_x(z)$ (x–z plane) and the elevational plane, $w_y(z)$ (y–z plane), respectively, for each of the three aspect ratios (see Table II). The source and homogeneous tissue medium quantities are listed in Table I save for the source diameter. Fig. 7 shows the spatial-average temporal-average intensity using a rectangular cross-sectional area. Fig. 8 shows the axial temperature increase profiles and Table II lists the maximum temperature increases and their axial locations.

V. Discussion

A. Monopole-Source Solution Modeling Parameters

A monopole-source spacing of $\lambda/4$ and a field spacing of 0.01 cm were used for the monopole-source solution. As the spacings are reduced, the axial temperature increase profiles improve in an asymptotic fashion. As indicated in Fig. 3(c), the maximum difference between the axial temperature increase profiles for the $\lambda/6$ and $\lambda/4$ spacing was -0.22% [see Fig. 3(c)]. The maximum difference between a field spacing of 0.01 and 0.005 cm was -0.22% [see Fig. 4(c)]. This level of tolerance was determined to be adequate. This idea is further illustrated by the results of Fig. 4(d)–(f) where the maximum

TABLE III
MAXIMUM TEMPERATURE INCREASES AND AXIAL LOCATION FOR HEATED-DISC AND MONOPOLE-SOURCE SIMULATIONS

	ΔT_{max} (°C)	ΔT_{max} range (cm)
Heated-disc Solution	0.501	1.12
Monopole-source Solution	0.517	1.14

difference between a field spacing of 0.001 and 0.005 cm was -0.30%.

B. Heated-Disc Versus Monopole-Source Solutions

A direct comparison of the monopole-source solution with the heated-disc model solution [15], [16] for an identical set of source and medium (Table I) parameters is shown in Fig. 5. In Fig. 5(c), the axial temperature increase profiles for both models for the circular aperture are very similar in both their maximum temperature increase and axial distance at which that occurs (see Table III).

However, near the focal region ($z \approx 6.5$ cm, see Fig. 5), the magnitudes of the axial temperature increase are different for the two models. The difference can be explained in terms of their beam widths [Fig. 5(a)]. The two beam widths are strikingly similar except for the distinct steps in the monopole-source solution beam width (solid line) around the focal region. This beam width difference correlates with a significant difference in the intensity profiles [Fig. 5(b)] for the two models. The large difference in the I_{SATA} values in the focal region indicates that the I_{SATA} maximum near the focal region for the heated-disc approach results from beam width modeling (14), not from the actual ultrasonic field. In addition, due to the fact that not all of the energy is contained within the 10-dB beam width, the magnitude of I_{SATA} is lower than that calculated as in the heated-disc method, where all of the energy, by definition, is contained within the selected beam width.

To test the hypothesis that the differences in the focal region of the temperature increase profiles [Fig. 5(c)] for the circular aperture are due to the beam width differences, the computed 10-dB beam width from the monopole-source solution is used as the beam width with the heated-disc approach. Fig. 9(a) shows the axial temperature increase profile calculated *with the heated disc method* for two beam widths, viz., that used by the heated-disc approach and that determined from the computed monopole-source solution of the ultrasonic field. Fig. 9(b) shows the axial temperature increase difference between the two temperature increase profiles. As suspected, the apparent "roughness" of the latter temperature increase profile (using the heated-disc approach with the computed 10-dB beam width) is due to the apparent "roughness" of the computed 10-dB beam width shown in Fig. 5(a).

From the p_0^2 distribution of the monopole-source solution, the 6-, 8-, 10-, and 12-dB beam widths as a function of axial distance, z, were determined [Fig. 10(a)], and the power contained within each beam width was determined [Fig. 10(b)].

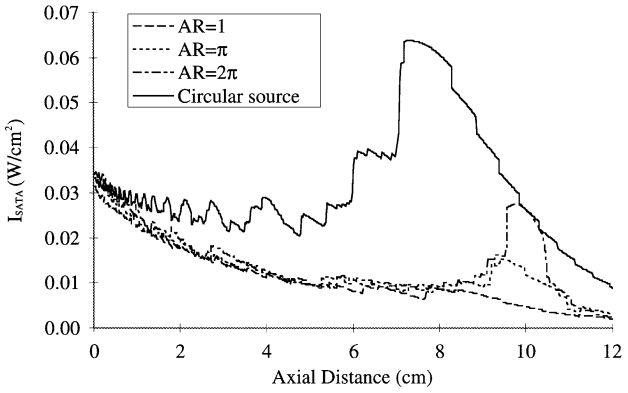

Fig. 7. The spatial-average temporal-average intensity calculated from the monopole-source solution for the circular aperture and the three aspect ratio (AR) rectangular aperture cases. For the circular aperture, the source and homogeneous tissue medium quantities are listed in Table I. For the rectangular apertures, the source and homogeneous tissue medium quantities are listed in Table I save for the source diameter; the rectangular source aperture dimensions are listed in Table II. The source aperture area is π cm^2 for all four cases.

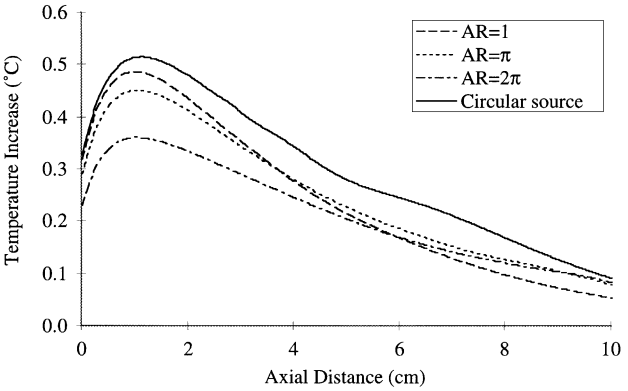

Fig. 8. Axial temperature increase profiles from the monopole-source solution for the circular aperture and the three aspect ratio (AR) rectangular aperture cases. For the circular aperture, the source and homogeneous tissue medium quantities are listed in Table I. For the rectangular apertures, the source and homogeneous tissue medium quantities are listed in Table I save for the source diameter; the rectangular source aperture dimensions are listed in Table II. The source aperture area and source power are π cm^2 and 100 mW, respectively, for all four cases.

The solid smooth line in Fig. 10(b) is the derated (by $A = 0.15$ Np/cm) power for a source power (W_{SOURCE}) of 100 mW, that is,

$$W(z) = W_{\mathrm{SOURCE}} \exp(-2Az) = 100 \exp(-0.30z) \text{ [mW]}. \quad (18)$$

For each of the four beam widths, the derated power $W_{\mathrm{BW}}(z)$ contained within the beam cross-sectional area $\mathrm{BA}(z)$ at range z is determined by summing all of the $p_0^2/(2\rho c)$ contributions within $\mathrm{BA}(z)$, that is,

$$W_{\mathrm{BW}}(z) = \frac{1}{2\rho c} \sum_{\mathrm{BA}(z)} p_0^2 \Delta x \Delta y. \quad (19)$$

Fig. 10(c) shows the difference between $W_{\mathrm{BW}}(z)$ and $W(z)$ where the percentage of power contained within each beam

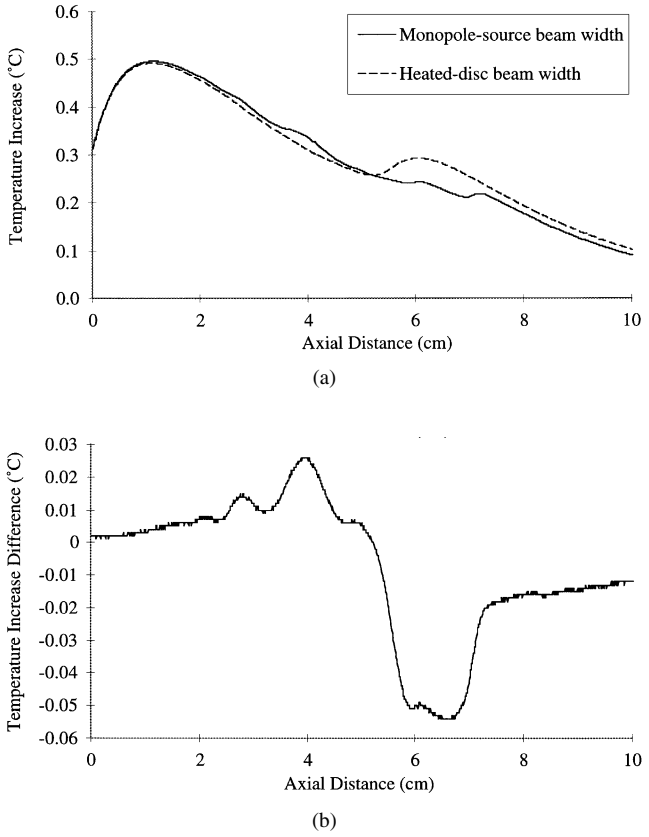

Fig. 9. (a) Axial temperature increase profiles calculated using the heated-disc approach for the two beam widths, viz., the 10-dB beam width determined from the computed monopole-source solution and the beam width used with the heated-disc solution (see Fig. 5(a), dashed line). The circular source and homogeneous tissue medium quantities are listed in Table I. (b) The axial temperature increase difference between the two temperature increase profiles.

area is determined from

$$\% \text{ Power within BW}(z) = \frac{W_{\text{BW}}(z)}{W(z)} \times 100. \qquad (20)$$

Note that at $z = 6.5$ cm, the 6-dB beam width contains approximately 33% of the total power.

Fig. 11(a) shows the power at $z = 6.5$ cm contained within a beam area where the beam area is defined by a circle with a radius which is the radial distance perpendicular to the beam axis. Note that as the radial distance increases (i.e., as the beam area increases), the power's asymptotic limit approaches about 14 mW, which is consistent with (18), that is, the total power is

$$W(z = 6.5 \text{ cm}) = 100 \exp(-0.30 \times 6.5) = 14.2 \text{ mW}. \quad (21)$$

The normalization of Fig. 11(a) to its asymptotic limit yields Fig. 11(b) where the percentage of total power at $z = 6.5$ cm as a function of beam area is shown.

In summary, the maximum temperature increase for a circular aperture focused transducer geometry is the same for both the heated-disc and the monopole-source solution for temperature increase for the parameters listed in Table I. However, the heated-disc approach alone does *not* accurately predict the temperature increase near the focal region. This is due to the modeling of the beam width near the focal region.

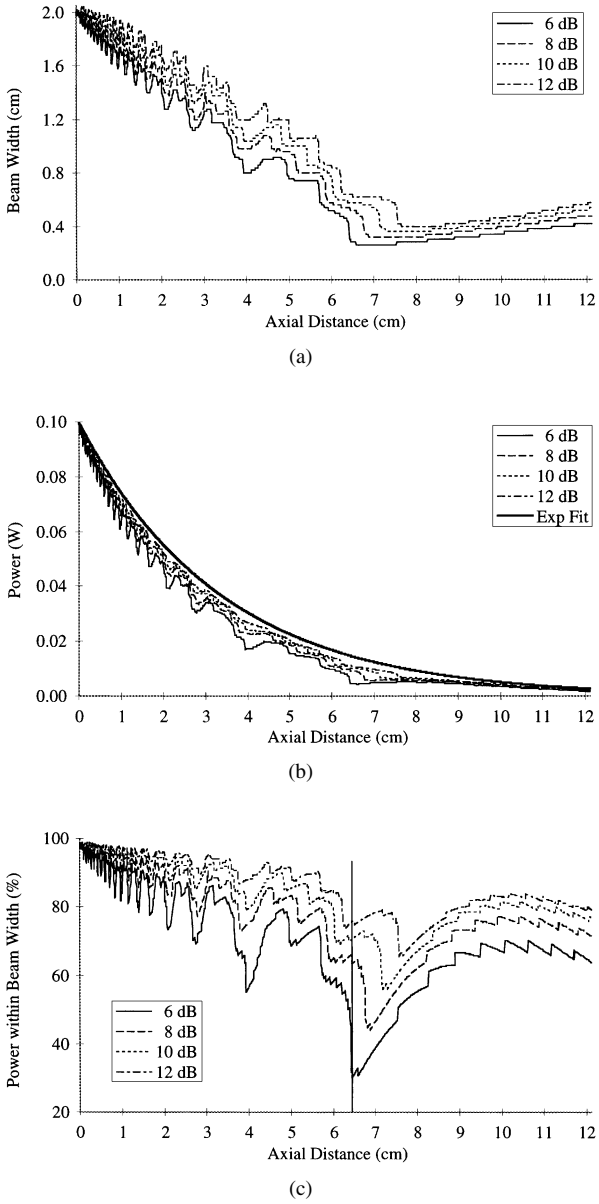

Fig. 10. (a) The 6-, 8-, 10-, and 12-dB beam widths as a function of axial distance for the circular source and homogeneous tissue medium quantities listed in Table I, (b) the power contained within each beam width as a function of axial distance, and (c) the normalized power contained within each beam width as a function of axial distance. The exponential fit in (b) is the derated (by 0.15 Np/cm) power for a source power of 100 mW, and the vertical line in (c) is located at an axial distance of 6.5 cm, where the normalized power contained within the 6-, 8-, 10-, and 12-dB beam widths are, respectively, 32.8, 64.5, 71.8, and 75.4%.

An important point to emphasize with the monopole-source solution is that the axial distribution of ΔT, and hence $\Delta T_{\max}$, is determined from the bio-heat transfer equation and the field distribution, p_0^2. The monopole-source solution does not require the independent use of the beam width as an input variable as does the heated-disc approach.

C. Rectangular Aperture

Comparison between the circular aperture case and the rectangular aperture case with several aspect ratios is shown

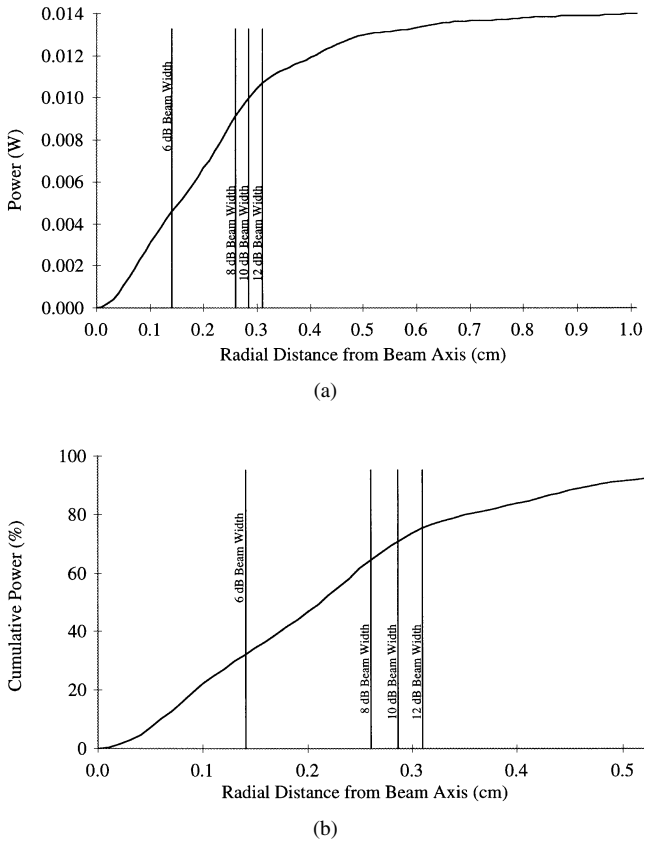

Fig. 11. (a) Power as a function of radial distance, that is, as a function of beam width, at an axial distance of $z = 6.5$ cm for the circular source and homogeneous tissue medium quantities listed in Table I where, for the 6-, 8-, 10-, and 12-dB beam widths, the powers contained within each beam width are 4.66, 9.16, 10.2, and 10.7 mW, respectively. The total power at an axial distance of 6.5 cm is 14.2 mW. (b) The percentage of total power as a function of radial distance at an axial distance of $z = 6.5$ cm.

in Fig. 8. The temperature increase profiles exhibit the same characteristics, viz., a singular maximum near an axial distance of 1.0 cm with the same general shape. The maximum temperature increase for the square aperture is slightly lower than for the circular aperture, by 0.016°C or 3.2% for the same aperture areas (see Table III). This small difference in the maximum temperature increase is attributed to the difference in the distribution of the point sources in that the distance from the four square corners are subjected to greater attenuation effects and to the geometry differences wherein the square source is focused only in the imaging plane. This is evident when examining I_{SATA} for the square aperture case as compared to that for the circular aperture case (Fig. 7). In Fig. 7, the axial I_{SATA} profile is given for the square aperture using the rectangular cross-sectional area. The difference in I_{SATA} and thus temperature increase can also be explained by the fact that circular aperture focusing is occurring in two dimensions while rectangular aperture focusing is occurring in one dimension.

An additional observation is that the relationship between the aspect ratio and the maximum temperature increase. As the aspect ratio increases, the distance from the corners of the aperture is further increased. Thus, due to attenuation, the resulting maximum axial temperature increase decreases as the aspect ratio increases (see Fig. 8).

VI. Conclusion

A generalized method for calculating the pressure distribution field and associated temperature increase profile in a homogeneous medium has been presented. The main feature of this method is its flexibility with the type of transducer as well as with tissue models. Previously published methods [15], [16] have been restricted to circular aperture transducers due to the complex computations required. The monopole-source solution does not require any ultrasound beam symmetry to calculate the temperature increase in tissue exposed to ultrasound. In addition, the method is not restricted to calculating the axial temperature increase. The temperature increase at any point in the medium may be determined.

The monopole-source solution has been compared to the accepted heated-disc method [15], [16] and produced the same maximum temperature increase results. In addition, the monopole-source solution has extended the ability to calculate the temperature increase to the case of the rectangular aperture. The relationship between the aspect ratio of the rectangular aperture transducer and the maximum temperature increase has been developed. As the aspect ratio of the rectangular transducer aperture increases, the maximum temperature increase decreases. Also, for the square aperture transducer, a slightly lower temperature increase than for the circular aperture case was shown.

References

[1] M. W. Miller and M. C. Ziskin, "Biological consequences of hyperthermia," *Ultrasound Med. Biol.*, vol. 15, no. 8, pp. 707–722, 1989.
[2] FDA, "501(k) guide for measuring and reporting acoustic output of diagnostic ultrasound medical devices," Ctr. Devices Radiological Health, U.S. Food Drug Admin., Rockville, MD, 1985.
[3] _____, "Revised 501(k) diagnostic ultrasound guidance for 1993," Ctr. Devices Radiological Health, U.S. Food Drug Admin., Rockville, MD, 1993.
[4] F. L. Lizzi and M. Ostromogilsky, "Analytical modeling of ultrasonically induced tissue heating," *Ultrasound Med. Biol.*, vol. 13, no. 10, pp. 607–618, 1987.
[5] F. L. Lizzi, J. Driller, B. Lunzer, A. Kalisz, and D. J. Coleman, "Computer model of ultrasonic hyperthermia and ablation for ocular tumors using B-mode data," *Ultrasound Med. Biol.*, vol. 18, no. 1, pp. 59–73, 1992.
[6] W. L. Nyborg, "Heat generation by ultrasound in a relaxing medium," *J. Acoust. Soc. Amer.*, vol. 70, no. 2, pp. 310–312, 1981.
[7] W. L. Nyborg and R. B. Steele, "Temperature elevation in a beam of ultrasound," *Ultrasound Med. Biol.*, vol. 9, no. 6, pp. 611–620, 1983.
[8] W. L. Nyborg and W. D. O'Brien, Jr., "An alternative simple formula for temperature estimates," *J. Ultrasound Med.*, vol. 8, pp. 653–654, 1989.
[9] R. B. Roemer, W. Swindell, S. T. Clegg, and R. L. Kress, "Simulation of focused, scanned ultrasonic heating of deep-seated tumors: The effect of blood perfusion," *IEEE Trans. Sonics Ultrason.*, vol. SU-31, no. 5, pp. 457–466, 1984.
[10] J. Wu and G. Du, "Temperature elevation generated by a focused Gaussian beam of ultrasound," *Ultrasound Med. Biol.*, vol. 16, no. 5, pp. 489–498, 1990.
[11] J. Wu, J. D. Chase, Z. Zhu, and T. P. Holzapfel, "Temperature rise in a tissue-mimicking material generated by unfocused and focused ultrasonic transducers," *Ultrasound Med. Biol.*, vol. 18, no. 5, pp. 495–512, 1992.
[12] J. Wu and W. L. Nyborg, "Temperature rise generated by a focussed Gaussian beam in a two-later medium," *Ultrasound Med. Biol.*, vol. 18, no. 3, pp. 293–302, 1992.
[13] T. J. Cavicchi and W. D. O'Brien, Jr., "Heat generated in an absorbing medium," *J. Acoust. Soc. Amer.*, vol. 76, pp. 1244–1245, 1984.
[14] World Federation for Ultrasound in Medicine and Biology (WFUMB), "Issues and recommendations regarding the thermal mechanisms for biological effects of ultrasound," *Ultrasound Med. Biol.*, vol. 7, no. 9, pp. 733–810, 1992.

[15] National Council on Radiation Protection and Measurements (NCRP), "Exposure criteria for medical diagnostic ultrasound: I. Criteria based on thermal mechanisms," Bethesda, MD, Rep. 113, 1992.
[16] American Institute of Ultrasound in Medicine (AIUM), Bioeffects Committee, "Biological considerations for the safety of diagnostic ultrasound," *J. Ultrasound Med.*, vol. 7, no. 10 (suppl.), pp. S8–S17, 1988.
[17] American Institute of Ultrasound in Medicine (AIUM), *Standard for Real-Time Display of Thermal and Mechanical Acoustic Output Indices on Diagnostic Ultrasound Equipment*. Rockville, MD: AIUM, 1992.
[18] W. L. Nyborg, "Solutions to the bio-heat transfer equation," *Phys. Med. Biol.*, vol. 33, no. 7, pp. 785–792, 1988.
[19] H. H. Pennes, "Analysis of tissue and arterial blood temperatures in the resting human forearm," *J. Appl. Physiol.*, vol. 1, no. 2, pp. 93–122, 1948.
[20] G. Kossoff, "Analysis of focusing action of spherically curved transducers," *Ultrasound Med. Biol.*, vol. 5, pp. 359–365, 1979.

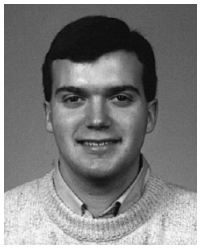

D. Scott Ellis was born in Evanston, IL on March 16, 1969. He received the B.S. and M.S. degrees in electrical engineering from the University of Illinois at Urbana-Champaign in 1991 and 1992, respectively.

He is currently with the Bioacoustic Research Laboratory at the University of Illinois at Urbana-Champaign. He was the recipient of a National Institutes of Health Radiation Oncology Trainee Fellowship in 1992. His research interests include ultrasound exposimetry and tissue heating.

Mr. Ellis is a member of Tau Beta Pi and Eta Kappa Nu.

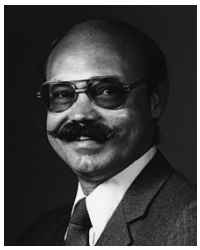

William D. O'Brien, Jr. (S'64–M'70–SM'79–F'89) received the B.S., M.S., and Ph.D. degrees in 1966, 1968, and 1970, from the University of Illinois, Urbana-Champaign.

From 1971 to 1975, he worked with the Bureau of Radiological Health (currently, the Center for Devices and Radiological Health) of the U.S. Food and Drug Administration. Since 1975, he has been at the University of Illinois, where he is a Professor of Electrical and Computer Engineering and of Bioengineering, College of Engineering, and a Professor of Bioengineering, College of Medicine. He is also the Director of the Bioacoustics Research Laboratory and the Program Director of the NIH Radiation Biophysics and Bioengineering in Oncology Training Program. His research interests involve the many areas of ultrasound–tissue interaction, including spectroscopy, risk assessment, biological effects, tissue characterization, dosimetry, blood-flow measurements, acoustic microscopy, and meat characterization, for which he has published more than 160 papers.

Dr. O'Brien is a Fellow of the Acoustical Society of America (ASA) and the American Institute of Ultrasound in Medicine (AIUM), and a Founding Fellow of the American Institute of Medical and Biological Engineering. He was the recipient of the IEEE Centennial Medal (1984), the AIUM Presidential Recognition Awards (1985 and 1992), the AIUM/WFUMB Pioneer Award (1988), the IEEE Outstanding Student Branch Counselor Award (1989), and the AIUM Joseph H. Holmes Basic Science Pioneer Award (1993). He has been President (1982–1983) of the IEEE Sonics and Ultrasonics Group (currently, the IEEE Ultrasonics, Ferroelectrics, and Frequency Control Society), Co-Chairman of the 1981 IEEE Ultrasonics Symposium, and General Chairman of the 1988 IEEE Ultrasonics Symposium. He has also been President of the AIUM (1988–1991) and Treasurer of the World Federation for Ultrasound in Medicine and Biology (1991–1994). He is currently Editor-in-Chief of the IEEE TRANSACTIONS ON ULTRASONICS, FERROELECTRICS, AND FREQUENCY CONTROL.